A Second SARS-CoV S2 Glycoprotein Internal Membrane-Active Peptide. Biophysical Characterization and Membrane Interaction†

Jaime Guillén, Ana J. Pérez-Berná, Miguel R. Moreno, and José Villalaín*

Instituto de Biología Molecular y Celular, Campus de Elche, Universidad "Miguel Hernández", E-03202 Elche-Alicante, Spain

Received May 5, 2008; Revised Manuscript Received June 9, 2008

ABSTRACT: The severe acute respiratory syndrome coronavirus (SARS-CoV) envelope spike (S) glycoprotein, a class I viral fusion protein, is responsible for the fusion between the membranes of the virus and the target cell. The S2 domain of protein S has been suggested to have two fusion peptides, one located at its N-terminus, downstream of the furin cleavage, and another, more internal, located immediately upstream of the HR1. Therefore, we have carried out a study of the binding and interaction with model membranes of a peptide corresponding to segment 873−888 of the SARS-CoV S glycoprotein, peptide $SARS_{IFP}$, as well as the structural changes taking place in both the phospholipid and the peptide induced by the binding of the peptide to the membrane. We demonstrate that $SARS_{IFP}$ peptide binds to and interacts with phospholipid model membranes and shows a higher affinity for negatively charged phospholipids than for zwitterionic ones. $SARS_{IFP}$ peptide specifically decreases the mobility of the phospholipid acyl chains of negatively charged phospholipids and adopts different conformations in the membrane depending upon their composition. These data support its role in SARS-mediated membrane fusion and suggest that the regions where this peptide resides might assist the fusion peptide and/or the pretransmembrane segment of the SARS-CoV spike glycoprotein in the fusion process.

Severe acute respiratory syndrome coronavirus (SARS-CoV)[1] is a newly emergent member in the family *Coronaviridae* that causes a severe infectious respiratory disease. Unlike other human coronaviruses whose infections are usually very mild, the SARS-CoV produced mortality rates as high as 10% but increased to greater than 50% in persons older than age 60 (*1*). Before SARS-CoV appeared, only two human coronaviruses (HCoV) were known, 229E and OC43, both causing about 30% of common colds. Since the SARS outbreak, two new human coronaviruses have been identified, HCoV-NL63 (*2*) and HCoV-HKU1 (*3*), both causing potentially severe respiratory infections. Five years after its identification, many of its pathological features remain to be characterized.

SARS-CoV infection, similarly to other envelope viruses, is achieved through fusion of the lipid bilayer of the viral envelope with the host cell membrane (*4*), although recent studies have shown that the entry of SARS-CoV into the cell may be also pH-dependent (*5*). The spike glycoprotein S, responsible for the characteristic spikes of the SARS-CoV, is a surface class I viral fusion glycoprotein that mediates viral entry by binding to the cellular receptor angiotensin-converting enzyme 2 (*6*) and induces membrane fusion. SARS-CoV S glycoprotein seems to be cleaved into S1 and S2 subunits (*7*), but cleavage is not an absolute requirement for the mechanism of fusion (*8*). The S1 subunit contains the receptor binding domain, whereas the S2 is responsible for the fusion between the viral and cellular membranes (*2, 9*). S2 contains two predicted α-helical heptad repeat regions (HR1 and HR2; see Figure 1) of the type found in several other fusion proteins which form coiled-coil structures (*10, 11*). Computer sequence predictions and systematic amino acid mapping studies of the S2 domain have located the HR1 region to amino acids from approximately 892 to 972, while the HR2 region extends from amino acids from approximately 1142 to 1184 (*2, 11, 12*). Binding of the S1 subunit to the receptor is thought to trigger a series of conformational changes in S2 that brings, via the formation of an antiparallel six-helix bundle by the HR regions, the putative fusion peptide and the transmembrane domain in close proximity (*13*). These structural rearrangements in the S protein

† This work was supported by Grant BFU2005-00186-BMC (Ministerio de Ciencia y Tecnología, Spain) to J.V. M.R.M. was a recipient of a predoctoral fellowship from Ministerio de Educación, Cultura y Deporte, Spain. A.J.P.-B. and J.G. are recipients of predoctoral fellowships from the Autonomous Government of the Valencian Community, Spain.

* Corresponding author. Tel: +34 966 658 762. Fax: +34 966 658 758. E-mail: jvillalain@umh.es.

[1] Abbreviations: BPS, bovine brain L-α-phosphatidylserine; CF, 5-carboxyfluorescein; Chol, cholesterol; di-8-ANEPPS, 4-(2-(6-(dioctylamino)-2-naphthalenyl)-(ethenyl)-1-(3-sulfopropyl)pyridinium inner salt; DMPA, 1,2-dimyristoyl-*sn*-glycero-3-phosphatidic acid; DMPC, 1,2-dimyristoyl-*sn*-glycero-3-phosphatidylcholine; DMPG, 1,2-dimyristoyl-*sn*-glycero-3-phosphatidylglycerol; DMPS, 1,2-dimyristoyl-*sn*-glycero-3-phosphatidylserine; DPH, 1, 6-diphenyl-1,3,5-hexatriene; EPA, egg L-α-phosphatidic acid; EPC, egg L-α-phosphatidylcholine; EPG, egg L-α-phosphatidylglycerol; ESM, egg sphingomyelin; FP, fusion peptide; HCV, hepatitis C virus; HIV, human immunodeficiency virus; HR, heptad repeat region; LPC, lyso-α-phosphatidylcholine; PA-DPH, 3-(4-(6-phenyl)-1,3,5-hexatrienyl)phenylpropionic acid; POPC, 1-palmitoyl-2-oleoyl-*sn*-glycero-3-phosphatidylcholine; POPE, 1-palmitoyl-2-oleoyl-*sn*-glycero-3-phosphatidylethanolamine; PTM, pretransmembrane domain; SARS-CoV, severe acute respiratory syndrome coronavirus; $SARS_{IFP}$, internal membrane-active peptide of SARS; T_m, temperature of the gel-to-liquid crystalline phase transition; TM, transmembrane domain; TMA-DPH, 1-(4-trimethylammoniumphenyl)-6-phenyl-1,3,5-hexatriene; TPE, egg trans-sterified L-α-phosphatidylethanolamine.

10.1021/bi800814q CCC: $40.75
Published on Web 07/11/2008

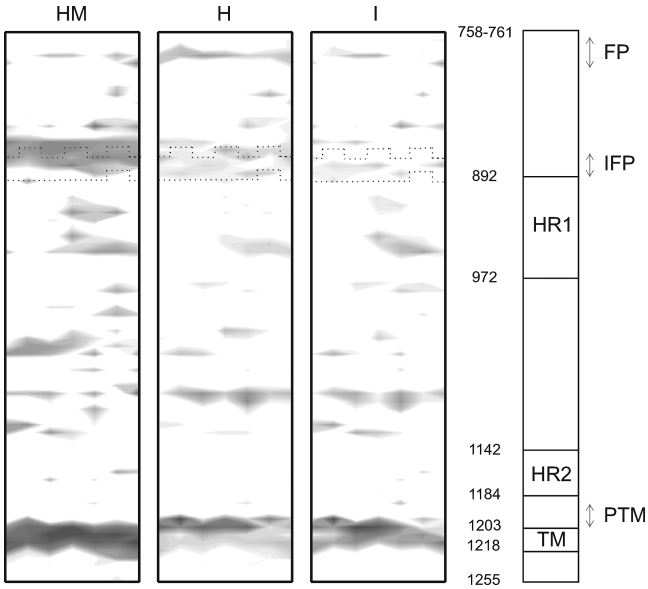

FIGURE 1: Positive bilayer-to-water transfer free energy values (shaded areas) for the hydrophobic moment (HM), hydrophobicity (H), and interfaciality (I) distribution along the SARS-CoV spike S2 protein, assuming it forms an α-helical wheel (see ref *24* for details), as well as a schematic view of the organization of SARS-CoV spike glycoprotein S2 (amino acid residues 758−1255 for the full length), showing the approximate structural and functional regions: the fusion domain FP, the predicted heptad repeat regions HR1 and HR2, the pre- and transmembrane domains (PTM and TM), and the relative position of the peptide used in this study ($SARS_{IFP}$). The exact location of the $SARS_{IFP}$ in the bidimensional plots is marked by dots.

generate the energy that drives the fusion of the viral and cellular lipid membrane. This fusion event releases the nucleocapsid into the host cell's cytoplasm.

Membrane fusion proteins share common motifs, one of them the fusion peptide (FP), a short segment rich in hydrophobic residues essential for fusion (*14, 15*). FPs also participate in inducing lipid rearrangements giving place to hemifusion and pore formation (*16, 17*) and are also involved in pore enlargement. In addition to classical FPs, different regions of the viral envelope glycoproteins are essential for membrane fusion to occur. These membrane-interacting regions are capable of modifying the biophysical properties of phospholipid membranes, suggesting that several segments may have a role in the fusion process (*18–22*). Although it has been predicted that the sequence comprising residues from 858 to 886 of the S2 domain of the SARS-CoV spike glycoprotein is the FP domain (*23, 24*), recent studies have shown that the region comprising residues 770−788 has a much more potent fusogenic activity than the former sequence and suggested to be the S2 FP (*25*). However, biophysical and mutagenesis studies have shown the importance of the 858−886 region, revealing its essential role in the spike glycoprotein mediated cell fusion: apart from having membrane-perturbing capacities (*24*), its mutation causes an inhibition of cell fusion by more than 70% (*26*).

Although much information has been obtained in recent years on membrane fusion, we do not know yet the processes and the mechanism behind virus−host cell membrane fusion. Elucidating the nature of the interactions between phospholipids, membrane proteins, and peptides is essential for the understanding of the structure and function of membrane proteins, clarifying the specific roles of specific types of phospholipids in biological membranes. Based on our recent work (*24*), and since this region of SARS-CoV S2 envelope glycoprotein might be involved in membrane destabilization and at the same time take part in the fusion events like a helper for the fusion peptide and/or the pretransmembrane regions, we have selected a specific sequence from the SARS-CoV sequence, amino acids 873−888, peptide $SARS_{IFP}$. We have made an in-depth study of $SARS_{IFP}$, aiming to elucidate the capacity of this region to interact and disrupt membranes, and our results demonstrate that this peptide binds and interacts differently with the membrane depending on the charge of the phospholipids, and the effect on the integrity and phase behavior of the membrane also depends on specific headgroup interactions. Moreover, the peptide adopts different structures depending on its environment. These results would suggest that $SARS_{IFP}$ could be involved in the merging of the viral and target cell membranes working synergistically with the other membrane-active regions of the SARS-CoV S2 glycoprotein.

MATERIALS AND METHODS

Materials and Reagents. A 16-residue peptide pertaining to the S2 domain of SARS-CoV (^{873}GAALQIPFAMQMAYRF^{888}, with N-terminal acetylation and C-terminal amidation) was obtained from Genemed Synthesis, San Francisco, CA. The peptide was purified by reverse-phase HPLC (Vydac C-8 column, 250 × 4.6 mm, flow rate 1 mL/min, solvent A, 0.1% trifluoroacetic acid, solvent B, 99.9 acetonitrile and 0.1% trifluoroacetic acid) to better than 95% purity, and its composition and molecular mass were confirmed by amino acid analysis and mass spectroscopy. Since trifluoroacetate has a strong infrared absorbance at approximately 1673 cm^{-1}, which interferes with the characterization of the peptide amide I band (27), residual trifluoroacetic acid, used both in peptide synthesis and in the high-performance liquid chromatography mobile phase, was removed by several lyophilization−solubilization cycles in 10 mM HCl. Egg phosphatidylcholine (EPC), egg phosphatidylglycerol (EPG), egg phosphatidic acid (EPA), egg sphingomyelin (ESM), bovine brain phosphatidylserine (BPS), egg trans-sterified phosphatidylethanolamine (TPE), bovine liver phosphatidylinositol (BPI), 1,2-dimyristoylphosphatidylcholine (DMPC), 1,2-dimyristoylphosphatidylglycerol (DMPG), 1,2-dimyristoylphosphatidylserine (DMPS), 1,2-dimyristoylphosphatidic acid (DMPA), cholesterol (Chol), 1-palmitoyl-2-oleoyl-*sn*-glycero-3-phosphoethanolamine (POPE), lyso-α-phosphatidylcholine (LPC), and 1-palmitoyl-2-oleoyl-*sn*-glycero-3-phosphatidylcholine (POPC) were obtained from Avanti Polar Lipids (Alabaster, AL). 5-Carboxyfluorescein (CF) (>95% by HPLC), deuterium oxide (99.9% by atom), Triton X-100, EDTA, and HEPES were purchased from Sigma-Aldrich (Madrid, Spain). 1,6-Diphenyl-1,3,5-hexatriene (DPH), 3-[4-(6-phenyl)-1,3,5-hexatrienyl]phenylpropionic acid (PA-DPH), and 1-(4-trimethylammoniumphenyl)-6-phenyl-1,3,5-hexatriene (TMA-DPH) were obtained from Molecular Probes (Eugene, OR). All other reagents used were of analytical grade from Merck (Darmstad, Germany). Water was deonized, twice-distilled, and passed through Milli-Q equipment (Millipore Ibérica, Madrid) to a resistivity higher than 18 MΩ·cm.

Vesicle Preparation. Aliquots containing the appropriate amount of lipid in chloroform/methanol (2:1 v/v) were placed in a test tube, the solvents removed by evaporation under a stream of O_2-free nitrogen, and finally, traces of solvents were eliminated under vacuum in the dark for more than 3 h. The lipid films were resuspended in an appropriate buffer and incubated either at 25 or 10 °C above the phase transition temperature (T_m) with intermittent vortexing for 30 min to hydrate the samples and obtain multilamellar vesicles. The samples were frozen and thawed five times to ensure complete homogenization and maximization of peptide/lipid contacts with occasional vortexing. Large unilamellar vesicles with a mean diameter of 0.1 μm for CF leakage experiments were prepared from multilamellar vesicles by the extrusion method (*28*) using polycarbonate filters with a pore size of 0.1 μm (Nuclepore Corp., Cambridge, CA). Small unilamellar vesicles were prepared from multilamellar vesicles using a Branson 250 sonifier (40W) equipped with a microtip until the suspension became completely transparent. Every 30 s, the samples were cooled for 90 s in ice to prevent overheating of the solution. The titanium particles released from the tip were removed by centrifugation at 15000 rpm at room temperature for 15 min. The phospholipid and peptide concentration were measured by methods described previously (*29, 30*).

Membrane Leakage Measurement. Large unilamellar vesicles with a mean diameter of 0.1 μm were prepared as indicated above in buffer containing 10 mM Tris, 20 mM NaCl, pH 7.4, and CF at a concentration of 40 mM. Nonencapsulated CF was separated from the vesicle suspension through a filtration column containing Sephadex G-75 (Pharmacia, Uppsala, Sweden), eluted with buffer containing 10 mM Tris, 100 mM NaCl, and 0.1 mM EDTA, pH 7.4. Leakage of intraliposomal CF was assayed by treating the probe-loaded liposomes (final lipid concentration, 0.125 mM) with the appropriate amounts of peptide on microtiter plates using a microplate reader (FLUOstar; BMG Labtech, Offenburg, Germany), each well containing a final volume of 170 μL stabilized at 25 °C. The medium in the microtiter plates was continuously stirred to allow the rapid mixing of peptide and vesicles. One hundred percent release was achieved by adding Triton X-100 to the microtiter plates to a final concentration of 0.5% (w/w). Fluorescence measurements were made initially with probe-loaded liposomes and then by adding peptide solution, and finally 100% release was achieved by adding Triton X-100 to the microtiter plates (final concentration of 0.5% (w/w)). For details see refs *18 and 31*.

Peptide Binding to Vesicles. The partitioning of the peptide into the phospholipid bilayer was monitored by the fluorescence enhancement of tyrosine by successive additions of small volumes of small lamellar vesicles to the peptide sample (5.4×10^{-5} M). Fluorescence spectra were recorded in a SLM Aminco 8000C spectrofluorometer with excitation and emission wavelengths of 282 and 304 nm, respectively, and 4 nm spectral bandwidths. Measurements were carried out in 20 mM HEPES, 50 mM NaCl, and 0.1 mM EDTA, pH 7.4. Intensity values were corrected for dilution, and the scatter contribution was derived from lipid titration of a vesicle blank. The partition coefficient, K_p, represents the amount of peptide in the bilayer as a fraction of the total peptide present in the system (*32*). The data were analyzed as previously described (*18*).

Steady-State Fluorescence Anisotropy. Multilamellar vesicles were formed in 100 mM NaCl, 0.05 mM EDTA, and 25 mM HEPES, pH 7.4. Aliquots of TMA-DPH, PA-DPH, or DPH in *N*,*N*′-dimethylformamide (2×10^{-4} M) were directly added into the lipid dispersion to obtain a probe/lipid molar ratio of 1/500. Samples were incubated for 15, 45, or 60 min when TMA-DPH, PA-DPH, or DPH was used, respectively, 10 °C above the gel-to-liquid crystalline phase transition temperature T_m of the phospholipid mixture. Afterward, the peptides were added to obtain a peptide/lipid molar ratio of 1:15 and incubated 10 °C above the T_m of each lipid for 1 h, with occasional vortexing. All fluorescence studies were carried using 5 mm × 5 mm quartz cuvettes in a final volume of 400 μL (315 μM lipid concentration). All of the data were corrected for background intensities and progressive dilution. The steady-state fluorescence anisotropy, $\langle r \rangle$, was measured with an automated polarization accessory using a Varian Cary Eclipse fluorescence spectrometer, coupled to a Peltier device for automatic temperature change. The data were analyzed as previously described (*18*).

Fluorescence Quenching of Tyr Emission by Acrylamide. For acrylamide quenching assays, aliquots from a 4 M solution of the water-soluble quencher were added to the solution-containing peptide (5.4×10^{-5} M) in the presence and absence of liposomes at a peptide/lipid molar ratio of 1:100. The results obtained were corrected for dilution, and the scatter contribution was derived from acrylamide titration of a vesicle blank. The data were analyzed according to the Stern−Volmer equation (*33*), $I_0/I = 1 + K_{sv}[Q]$, where I_0 and I represent the fluorescence intensities in the absence and the presence of the quencher [Q], respectively, and K_{sv} is the Stern−Volmer quenching constant.

Infrared Spectroscopy. For infrared spectroscopy, the samples were prepared as above but in D_2O buffer. Approximately 25 μL of a pelleted sample in D_2O buffer containing 20 mM HEPES, 50 mM NaCl, and 0.1 mM EDTA, pH 7.4, was placed between two CaF_2 windows separated by 50 μm thick Teflon spacers in a liquid demountable cell (Harrick, Ossining, NY). The spectra were obtained in a Bruker IFS55 spectrometer using a deuterated triglycine sulfate detector. Each spectrum was obtained by collecting 200 interferograms with a nominal resolution of 2 cm^{-1}, transformed using triangular apodization, and in order to average background spectra between sample spectra over the same time period, a sample shuttle accessory was used to obtain sample and background spectra. The spectrometer was continuously purged with dry air at a dew point of −40 °C in order to remove atmospheric water vapor from the bands of interest. All samples were equilibrated at the lowest temperature for 20 min before acquisition. An external bath circulator, connected to the infrared spectrometer, controlled the sample temperature. For temperature studies, samples were scanned using 2 °C intervals and a 2 min delay between each consecutive scan. The data were analyzed as previously described (*18, 31*).

Magic Angle Spinning (MAS) ^{31}P NMR. Samples were prepared as described above and concentrated by centrifugation (14000 rpm for 15 min). MAS ^{31}P NMR spectra were acquired on a Bruker 500 MHz Avance spectrometer (Bruker

BioSpin, Rheinstetten, Germany) using a Bruker 4 mm broad-band MAS probe under both static and MAS conditions. The samples were packed into 4 mm zirconia rotors and placed in the spinning module of the MAS probe; no cross-polarization was used. The spinning speed was 9 kHz, regulated to ±3 Hz by a Bruker pneumatic unit, and the temperature was 25 °C. A single ^{31}P 90° pulse (typically 5 μs) was used for excitation, a gated broad-band decoupling of 10 W, 32K data points, 1600 transients, and 5 s delay time between acquisitions. Under static conditions, the samples showed a broad asymmetrical signal with a low-frequency peak and a high-frequency shoulder characteristic of bilayer structures (data not shown).

Circular Dichroism Measurements. Circular dichrosim spectra were recorded at 25 °C using a JASCO-810 spectropolarimeter in a 2 mm path-length quartz cell. An external bath circulator Neslab RTE-111, connected to the spectropolarimeter, controlled the sample temperature. Wavelength spectra were acquired every 0.2 nm at a scan speed of 50 nm·min^{-1} with a response time of 2 s and averaged over five scans from 250 to 190 nm, with a bandwidth of 2 nm. Secondary structure predictions were estimated using the CDPro program suite (SELCON3, CONTIN/LL, and CDSSTR) (*34–36*). Spectra were corrected for the blank. Samples contained 40 μM peptide in 10 mM phosphate buffer at pH 7.4. Different concentrations of TFE, SDS, and LPC were added to the corresponding peptide samples.

RESULTS

SARS-CoV infection is achieved through fusion of the lipid bilayer of the viral envelope with the host cell plasma membrane, and the S2 glycoprotein is thought to be responsible for the fusion (*4*). Interestingly, recent studies have shown that the entry of SARS-CoV into the cell may be also pH-dependent, likely through a process requiring lipid rafts (*5*). We have shown the existence of different membranotropic regions of the SARS-CoV spike glycoprotein (*24*). In Figure 1 we present the analysis of the hydrophobic moment, hydrophobicity, and interfaciality distribution along the S2 glycoprotein sequence of SARS-CoV assuming it forms an α-helical wheel along the whole sequence (*24*). These data display the potential surface zones that could be implicated in the modulation of membrane binding and/or protein interaction. As we have shown previously, SARS-CoV S2 includes a highly membranotropic region located immediately upstream of HR1, which is localized in a similar place as the FP of HIV gp41 glycoprotein (*19*). Since this region could be important in the membrane fusion process (*37*), we present here the results of the study of the interaction of a peptide derived from this region with model membranes, the $SARS_{IFP}$ peptide, comprising residues 873−888 (Figure 1). This sequence could behave as a second fusion peptide of the SARS S2 glycoprotein.

The $SARS_{IFP}$ peptide contains a single tyrosine but no tryptophan. The use of intrinsic fluorescence of tyrosine is unusual to explore the interaction of peptides and proteins with lipid membranes, mainly because of the low fluorescence quantum yield, low extinction coefficient, and low sensitivity to changes in the surrounding environment. Despite this fact, it is possible to use the intrinsic fluorescence and anisotropy of the tyrosine residue to study the interaction and insertion of peptides in model membranes (*38*). The increase in fluorescence emission intensity of the Tyr residue of the $SARS_{IFP}$ peptide as a function of increasing lipid concentration is shown in Figure 2A. From data fitting, partition coefficients, K_p, were obtained for the different phospholipid compositions. Large K_p values in the 10^5-10^6 range were obtained for model membranes containing negatively charged phospholipids and lower but significant values in the case of zwitterionic membranes (10 (*4*) range). These K_p values show that the peptide (a) was bound to the membrane surface with high affinity and (b) interacted stronger with membranes containing negatively charged phospholipids but also with zwitterionic ones (*39*). The stronger interaction with negatively charged phospholipid-containing membranes was also corroborated by the larger increase in anisotropy of the Tyr residue of the peptide in the presence of negatively charged membranes whereas it was invariant or even slightly decreased, possibly owing to a scatter effect at high lipid/peptide ratios, in the presence of zwitterionic ones (Figure 2B). These data would indicate a significant motional restriction of the Tyr moiety of the peptide in the presence of negatively charged membranes (*40*).

To investigate the accessibility of membrane-bound $SARS_{IFP}$ peptide to the aqueous medium, we studied the accessibility of its Tyr residue toward acrylamide, a neutral, water-soluble, highly efficient quencher, which is unable to penetrate the hydrophobic core of the lipid bilayer to a large extent. The quenching data are presented in Figure 2C, and the resultant Stern−Volmer plots reveal that in aqueous solution the Tyr residue was highly exposed to the solvent that led to a more efficient quenching. However, in the presence of model membranes, the extent of quenching was significantly reduced, indicating a poor accessibility of the Tyr residue to the aqueous phase, consistent with the incorporation of the $SARS_{IFP}$ peptide into the lipid bilayer. As expected, K_{sv} values were lower in the presence of negatively charged phospholipids than in the presence of zwitterionic ones (see below). The linear Stern−Volmer plots indicate that the Tyr residue is fairly accessible to acrylamide.

In order to assess the effect of the $SARS_{IFP}$ peptide in the destabilization of membrane vesicles, we studied their effect on the release of encapsulated CF in model membranes made up of various compositions. The extent of leakage observed at different peptide-to-lipid molar ratios and the effect on different phospholipid compositions are shown in Figure 2D. It can be observed that $SARS_{IFP}$ was able to induce the release of the internal contents of the liposomes in a dose-dependent manner, but the absolute values of leakage were lower than those observed for other peptides, since in no case 100% of leakage was observed (*41*). At the highest lipid/peptide ratio used, the highest percentage of leakage (57%) was observed for the sample containing EPC/ESM/Chol. Lower, but significant, leakage values were obtained for liposomes composed of EPC and EPG (43% and 30%, respectively). Liposomes composed of EPA and EPC/BPS/Chol were the ones that elicited the lowest leakage values, i.e., about 11% (Figure 2D). In contrast to the results shown above, the highest leakage values were found for liposomes containing zwitterionic phospholipids, indicating that the $SARS_{IFP}$ peptide affects more significantly the integrity of

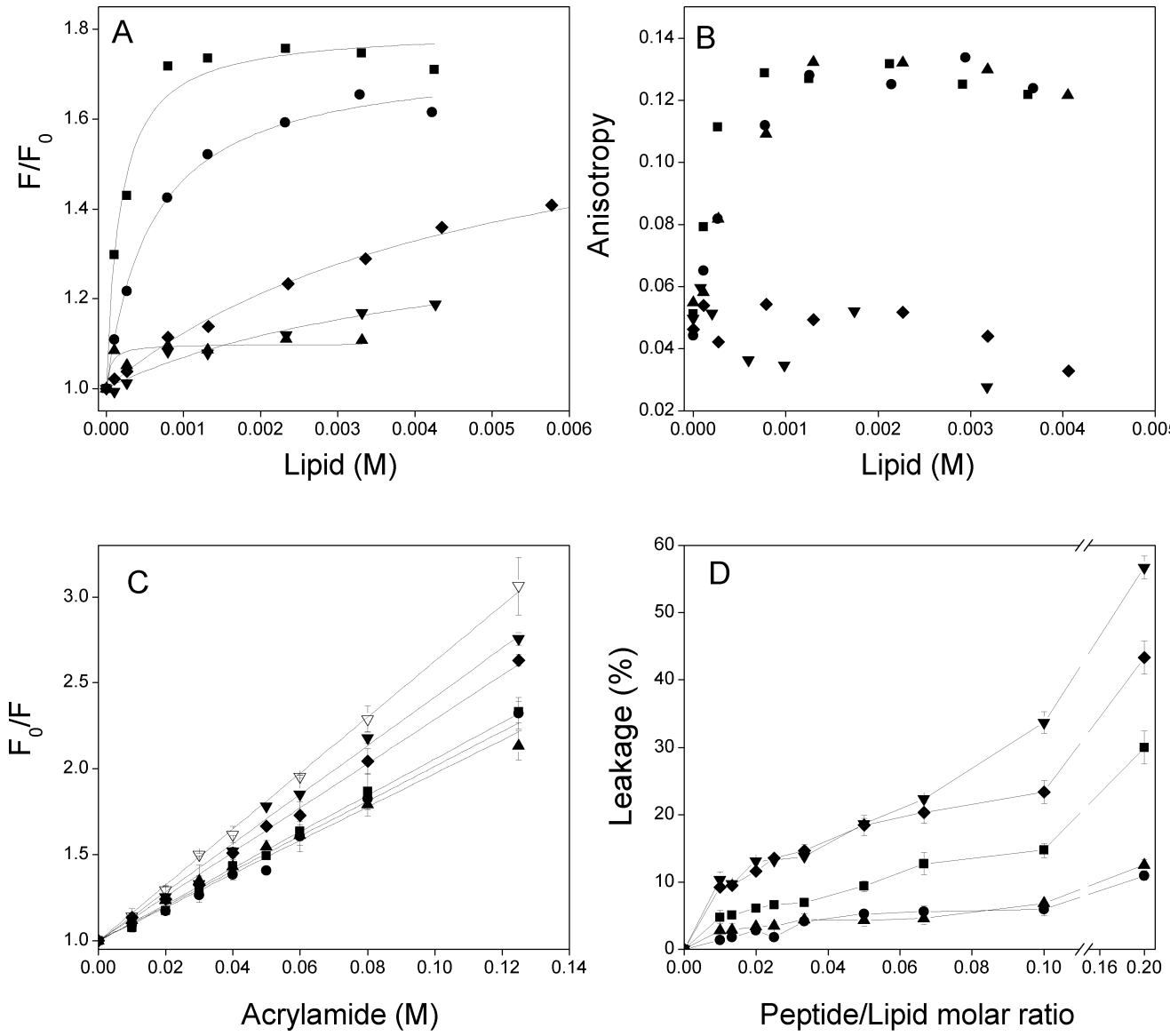

FIGURE 2: Change on the fluorescence intensity (A) and steady-state anisotropy (B) of the Tyr residue of the $SARS_{IFP}$ peptide in the presence of increasing lipid concentrations, (C) Stern−Volmer plots of the quenching of the Tyr fluorescence emission of $SARS_{IFP}$ by acrylamide in aqueous buffer (▽) and in the presence of liposomes, and (D) effect of the $SARS_{IFP}$ peptide on CF leakage in large unilamellar vesicles at different lipid-to-peptide molar ratios. The lipid compositions used were EPG (■), EPA (▲),EPC (♦), and EPC/BPS/Chol at a molar ratio of 5:3:1 (●) and EPC/ESM/CHOL at a molar ratio of 5:3:1 (▼).

membranes containing zwitterionic phospholipids rather than those containing negatively charged ones.

The effect of the $SARS_{IFP}$ peptide on the structural and thermotropic properties of phospholipid membranes was investigated by measuring the steady-state fluorescence anisotropy of the fluorescent probes DPH, PA-DPH, and TMA-DPH (*42*) incorporated into model membranes composed of saturated synthetic phospholipids as a function of temperature (Figure 3). The presence of the peptide did not induce any significant effect on the anisotropy of the fluorescent probes in the case of the neutral lipids DMPC and POPE, neither in the cooperativity of the transition nor on the anisotropy values below and above it (Figure 3A−C and 3D−F, respectively). However, in the case of the negative phospholipids DMPG, DMPS, and DMPA, the presence of the $SARS_{IFP}$ peptide mainly affected the anisotropy values of PA-DPH and DPH above the transition temperature. These data would indicate that $SARS_{IFP}$ affect mainly the phospholipid acyl chains of negatively charged phospholipids in the liquid crystalline phase but not in the gel phase, inducing a higher order in the chain packing. The reason that the anisotropy of TMA-DPH is only slightly affected is not clear. A possible explanation would be that the positively charged TMA-DPH probe could be moved away from the positive charge of the peptide, whereas this would not be the case for negatively charged (PA-DPH) and neutral (DPH) probes. However, it should not be ruled out that the effect observed on the DPH and PA-DPH anisotropy could be due to a change in the lifetime of these probes.

Although it has been shown that the incorporation of transmembrane peptides in the phospholipid palisade of the membrane can affect not only the phospholipid chain order but also interchain coupling, a shift in the frequency of the CH_2 and the CD_2 symmetric stretching band is a reliable index of the phase behavior of phospholipid dispersions since it can be used to monitor the average *trans/gauche* isomerization of the system (*43*). In order to discard the possible change in the lifetimes of the DPH fluorescent probes, we

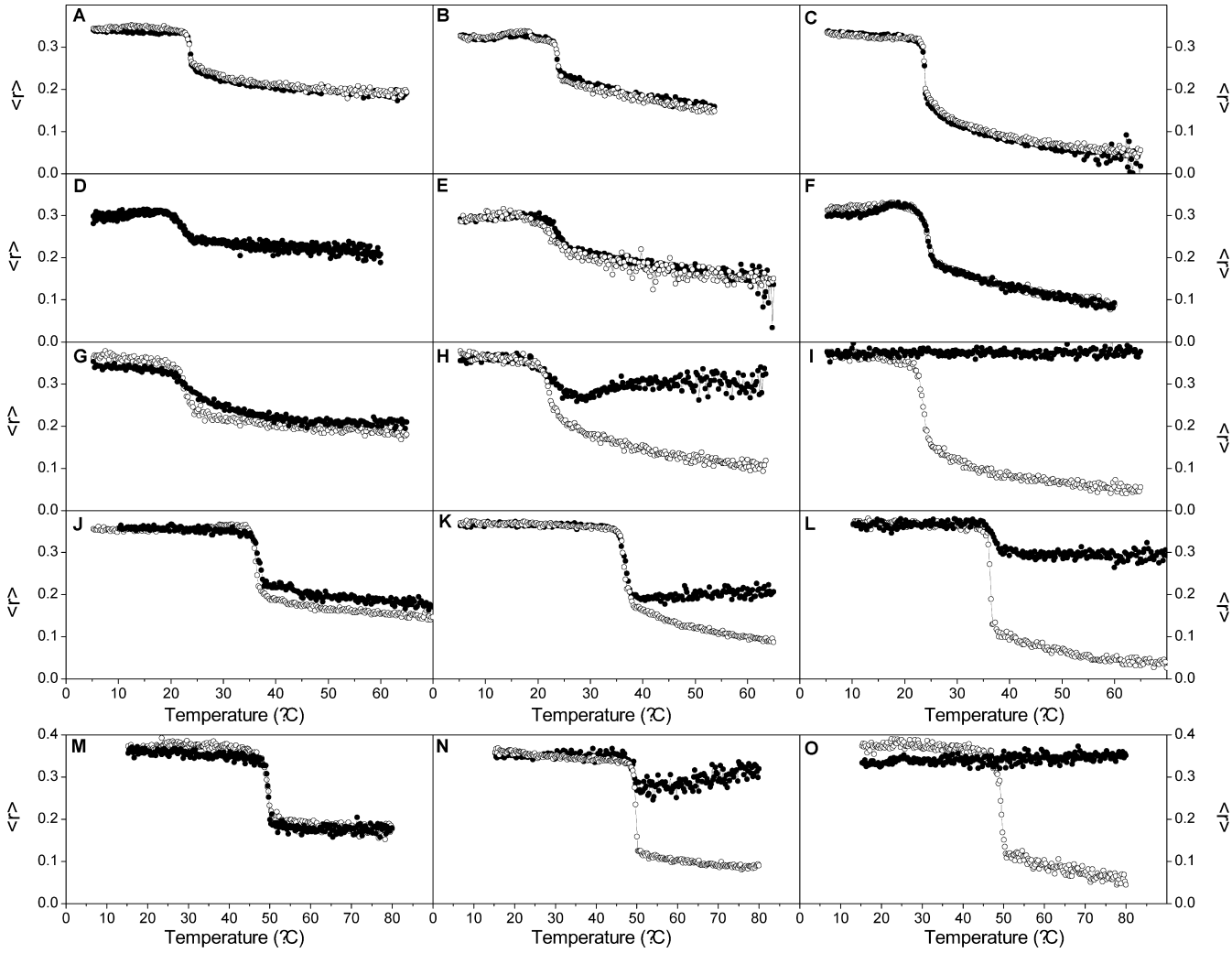

FIGURE 3: Steady-state anisotropy, $\langle r \rangle$, of the fluorescent probes TMA-DPH (A, D, G, J, and M), PA-DPH (B, E, H, K, and N), and DPH (C, F, I, L, and O) incorporated into model membranes composed of (A−C) DMPC, (D−F) POPE, (G−I) DMPG, (J−L) DMPS, and (M−O) DMPA model membranes as a function of temperature. Data correspond to vesicles in the absence (○) and in the presence of the $SARS_{IFP}$ peptide (●).

have studied the perturbations exerted by the $SARS_{IFP}$ peptide in the phospholipid acyl chain order by observing the changes in the frequency of the symmetric stretching bands of the phospholipids. The temperature dependence of the CH_2 symmetric frequency of pure DMPC is shown in Figure 4A, where a highly cooperative change at approximately 23 °C was observed, corresponding to the gel-to-liquid crystalline phase transition, T_m, of the phospholipid. In the presence of the peptide, the frequency of the CH_2 symmetric stretching band frequency both below and above the T_m increased, indicating that the incorporation of the peptide increased the proportion of *gauche* isomers, more significantly above T_m, characteristic of conformationally disordered acyl chains. Moreover, a small decrease in the gel-to-liquid crystalline phase transition was observed compared with the pure phospholipids, indicating a slight perturbation of the membrane by the peptide incorporation. Similar membrane disordering effects have been described for other viral fusion peptides, like the SIV fusion peptide (*44*), the feline leukemia fusion peptide (*45*), or the CDV fusion peptide (*46*). Panels B and C of Figure 4 display the CH_2 symmetric frequency of pure DMPG and DMPA, respectively, where a decrease of the frequency was observed, characteristic of an increase of the proportion of *trans* isomers, i.e., the hydrocarbon chains of the phospholipids were more ordered in the presence of the peptide. This decrease was observed both below and above the T_m for DMPA, but no effect on the cooperativity of the transition was observed. However, this decrease was observed only above the T_m for DMPG but jointly with a decrease in the cooperativity of the transition.

We have also studied the effect of the $SARS_{IFP}$ peptide in phospholipid binary mixtures where the acyl chains of one phospholipid was perdeuterated ($DMPC_d$), and the other, either DMPG or DMPA, was not, so that it was possible to detect independent changes in each phospholipid type. The CH_2 and CD_2 symmetric stretching frequencies of DMPA and $DMPC_d$ in the binary mixture $DMPC_d$/DMPA at a molar ratio of 1:1 are shown Figure 4D,F, whereas the CH_2 and CD_2 symmetric stretching frequencies of DMPG and $DMPC_d$ in the binary mixture $DMPC_d$/DMPG at a molar ratio of 1:1 are shown in Figure 4E,G. In both cases, the presence of the $SARS_{IFP}$ peptide induced a decrease in the CH_2 symmetric stretching band frequency of both DMPA and DMPG, in contrast to the little or no change in the CD_2 symmetric stretching band frequency of $DMPC_d$ in both samples. This specific effect of the $SARS_{IFP}$ peptide on negatively charged

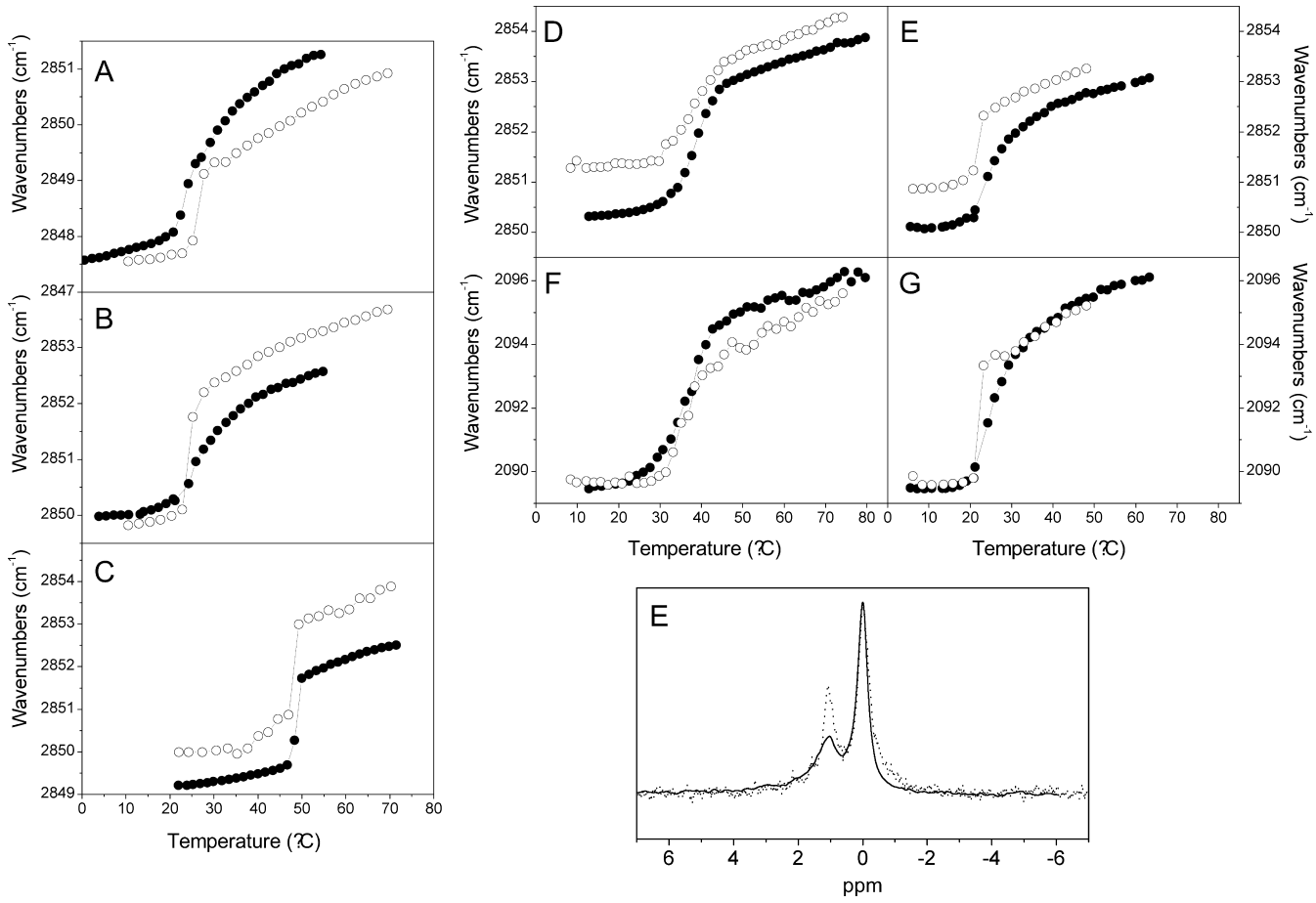

FIGURE 4: Dependence with temperature of the CH_2 symmetric stretching band frequency of (A) pure DMPC, (B) pure DMPG, (C) pure DMPA, (D) DMPA in an equimolar mixture of $DMPC_d$/DMPA, (E) DMPG in an equimolar mixture of $DMPC_d$/DMPG, and the CD_2 symmetric stretching band frequency of (F) $DMPC_d$ in an equimolar mixture of $DMPC_d$/DMPA and (G) $DMPC_d$ in an equimolar mixture of $DMPC_d$/DMPG, in the absence (○) and in the presence of $SARS_{IFP}$ peptide (●) at a phospholipid/peptide molar ratio of 15:1. (E) ^{31}P-MAS NMR at 25 °C and 9 kHz spinning speed (500 MHz proton frequency) spectra for POPC/EPA (2:1 molar ratio) in the absence (•••) and in the presence of the $SARS_{IFP}$ peptide at a phospholipid/molar ratio of 20:1 (—).

phospholipids but not on the zwitterionic ones in binary phospholipid mixtures, similarly to what was found with the pure ones, confirms its specific affinity for those phospholipids.

We have used ^{31}P-MAS NMR to observe the mixture POPC/EPA at a molar ratio of 2:1 since the ^{31}P NMR isotropic chemical shifts of both POPC and EPA headgroups are resolvable under MAS conditions. Furthermore, their spectral intensities reflect the molar ratio of each lipid in the mixture, and in this way, we can observe the line widths of each phospholipid component in the binary mixture. As observed in Figure 4E, the chemical shifts of the ^{31}P resonances of both POPC and EPA were not different both in the absence and in the presence of the $SARS_{IFP}$ peptide, but their line widths and relative intensities were dissimilar. In the absence of $SARS_{IFP}$, the ^{31}P line width at half-height of POPC was 87 Hz and that of EPA was 91 Hz, but these values shifted to 80 and 181 Hz, respectively, when the peptide was present. These results show that specifically EPA, a negatively charged phospholipid, but not POPC, a zwitterionic one, exhibits a lower degree of mobility and/or an increased heterogeneity of the headgroup environment in the presence of the peptide (*47*).

The existence of structural changes on the $SARS_{IFP}$ peptide induced by membrane binding has been studied by looking at the infrared amide I′ band located between 1700 and 1600 cm^{-1}. The infrared spectrum of the amide I′ region of the fully hydrated peptide in D_2O buffer at different temperatures is shown in Figure 5A. The spectrum was formed by different underlying components that gave place to two main bands, one of them located at about 1620 cm^{-1} and the other one at about 1644 cm^{-1}. Their intensity changed as the temperature increased; i.e., at low temperatures the more intense band appeared at 1620 cm^{-1} whereas at high temperatures the more intense band was the one located at 1644 cm^{-1}. Whereas the broad band at about 1644 cm^{-1} would correspond to a mixture of helical and unordered structures, the narrow band at about 1620 cm^{-1} accompanied by high wavenumber counterparts at 1680−1685 cm^{-1} would correspond to self-aggregated peptides forming a intermolecular network of hydrogen-bonded β-structures (*48*). The infrared spectra in the amide I′ region of the $SARS_{IFP}$ peptide in the presence of DMPC, DMPG, and DMPA at phospholipid/peptide molar ratios of 15:1 are shown in Figure 5B−D, respectively. The amide I′ region of the peptide in the presence of DMPC was very similar to that one of the peptide in solution, whereas it was significatively different in the presence of both DMPG and DMPA, since in the last case there was a main band at 1618 cm^{-1} with low intensity bands at about 1628 and 1655 cm^{-1}. It is interesting to note that the amide I′ region of the peptide in the presence of the negatively charged phospholipids did not change with temperature. In addition, we tested the effect of an increased

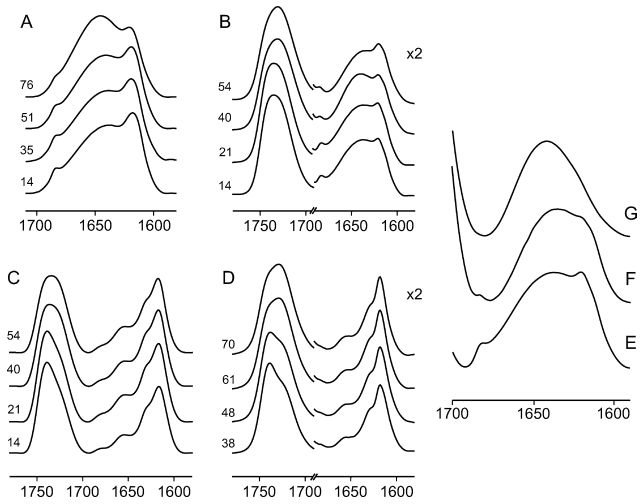

FIGURE 5: Stacked infrared spectra of the amide I′ and C═O regions of samples containing the $SARS_{IFP}$ peptide in solution (A) and in the presence of DMPC (B), DMPG (C), and DMPA (D) at different temperatures as indicated. The phospholipid-to-peptide molar ratio was 15:1. Spectra of the amide I′ region of the $SARS_{IFP}$ peptide in the presence of DMPC at a phospholipid/peptide molar ratio of (E) 15:1, (F) 75:1, and (G) 100:1, taken at T_m + 10 °C.

phospholipid/peptide molar ratio in order to check the influence of the lipid to peptide ratio on the secondary structure of the peptide (Figure 5E−G). As observed in the panels E−G, the bands at approximately 1620 and 1680 cm^{-1} disappeared at high lipid to peptide ratios, from which it can be inferred that a peptide disaggregation occurred. In the case of DMPG and DMPA there were no significant changes observed (not shown). These results imply that the secondary structure of the $SARS_{IFP}$ peptide was affected by the phospholipid composition of the membrane.

The secondary structure of the $SARS_{IFP}$ peptide was also analyzed by circular dichroism in different lipid mimetic media (Figure 6). In aqueous buffer the predominant structures were unordered and β-strand structures, in accordance with the infrared data shown above. The presence of increasing concentrations of TFE induced an increase of the content of α-helical structure (about 75% at 60% TFE; see Figure 6A). A similar behavior was observed at increasing concentrations of SDS (about 55% α-helical structure at 4 mM SDS and LPC at a phospholipid-to-peptide ratio of 50:1; see panels B and C of Figure 6, respectively). These data show the great flexibility and capability of the $SARS_{IFP}$ peptide to adopt different structures depending on the surrounding media, which it could be important in an energetically unfavorable process as membrane fusion is.

DISCUSSION

The fusion of the viral and cellular membranes is mediated by envelope fusion glycoproteins located on the outer surface of the viral membranes. Whereas class I membrane fusion proteins possess a fusion peptide at or near the amino terminus and a high α-helical content, class II fusion proteins possess an internal fusion peptide located at a distal location from the transmembrane anchor, as well as different domains comprised mostly of antiparallel β-sheets (*49, 50*). Their three-dimensional structure is different but their function is identical, so that they must share structural and functional characteristics in specific domains which interact with and disrupt biological membranes. Coronavirus spike proteins have many of the characteristics of the class I fusion proteins. Trimers of the S protein protrude from the virion envelope, giving place to its characteristic corona-like appearance. Like other class I fusion proteins, they have two HR regions in the S2 membrane subunit (*51*), which assemble into a stable, antiparallel heterotrimeric six-helix bundle (*10, 52*). Similar to what has been found for other class I fusion proteins, such a conformation in the full-length structure implies a colocalization of the fusion peptide predicted to occur N-terminally of HR1 and the viral transmembrane anchor, located C-terminally of HR2. This common structure is thought to facilitate membrane fusion by bringing the target membrane and viral membrane together. SARS-CoV S protein has a large ectodomain, more similar to the paramyxovirus envelope glycoproteins than to the orthomyxovirus and retrovirus. So, additional membrane binding regions seem to be necessary to complete the fusion process. In fact, a number of research works on membrane fusion proteins point out that there are several regions within these proteins that are involved in the fusion process and are decisive for membrane fusion to take place (*53*). On the basis of our recent work (*24*), we have selected a specific sequence from the SARS-CoV S2 sequence, amino acids 873−888, $SARS_{IFP}$. Consequently, we have made a comprehensive study of peptide $SARS_{IFP}$, characterizing its binding and interaction with model membrane systems.

The selected sequence of this work has been shown to have membrane-active properties in our recent work (*24*); accordingly, the $SARS_{IFP}$ peptide studied in this work displays a high binding constant to model membranes having different phospholipid compositions as has been found for other peptides (*18, 31*). $SARS_{IFP}$ showed a higher affinity for anionic phospholipid compositions than those containing zwitterionic phospholipids. The existence of a specific interaction with liposomes containing negatively charged phospholipids was corroborated by hydrophilic probe quenching, suggesting that the $SARS_{IFP}$ peptide was effectively incorporated in the membranes. Nevertheless, the $SARS_{IFP}$ peptide is capable of binding with high affinity to model membranes containing both negatively charged and zwitterionic phospholipids. $SARS_{IFP}$ was also capable of disrupting the membrane bilayer causing the release of fluorescent probes. This effect was dependent on the lipid composition and on the lipid/peptide molar ratio, being the highest effect observed for liposomes containing zwitterionic phospholipids. Lower but significant values were observed for liposomes containing negatively charged phospholipids. This effect could be due to the strong interaction between the peptide and the negatively charged phospholipids, resulting in peptide aggregation and consequently low leakage values.

We have also shown that $SARS_{IFP}$ peptide is capable of affecting the steady-state fluorescence anisotropy of fluorescent probes located in the membrane, since the peptide was able of decreasing the mobility of the phospholipid acyl chains of negatively charged phospholipids above but not below T_m when compared to the pure phospholipids. This specific effect on negatively charged phospholipids was corroborated by monitoring the frequency of the symmetric stretching bands of the phospholipid acyl chains, even in binary mixtures of negatively charged and zwitterionic phospholipids. Additionally, we showed by MAS NMR that

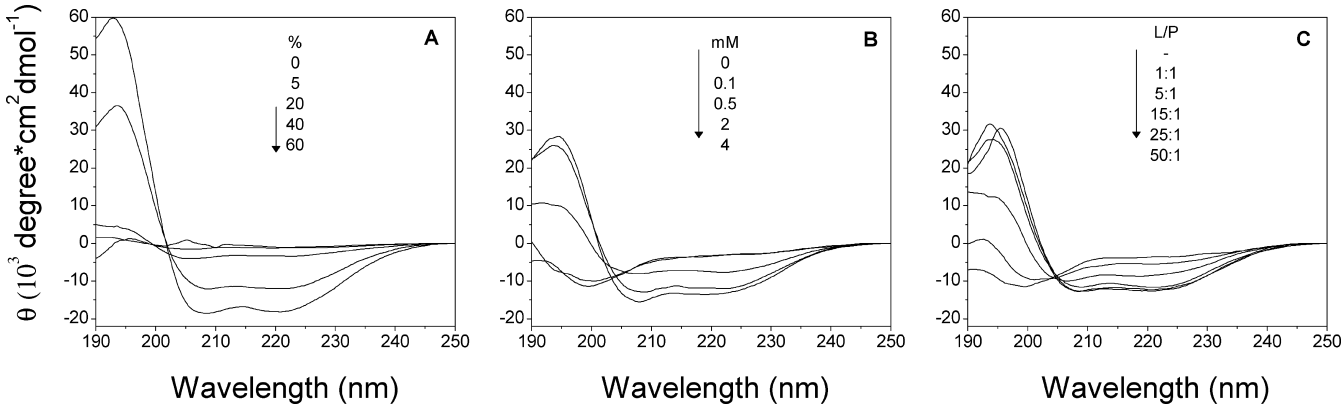

FIGURE 6: Circular dichroism spectra of the $SARS_{IFP}$ peptide in TFE (A), SDS (B), and LPC (C). The percentages of TFE, the SDS concentration in mM, and the LPC-to-peptide ratio are indicated. The temperature was 25 °C.

that the phosphate group of negatively charged phospholipid in binary mixtures displayed a lower degree of mobility in the presence of the $SARS_{IFP}$ peptide. Even so, the peptide has a disordering and perturbing effect in zwitterionic phospholipids, in agreement with the leakage data. The infrared spectra of the amide I′ region of the fully hydrated peptide did change with temperature, indicating a low stability of its conformation, where a mixture of α-helix, random, and aggregated structures coexisted. Interestingly, we have observed differences on the proportion of the different secondary elements when the peptide was incorporated into membranes of different phospholipid compositions and different peptide-to-lipid molar ratios. Whereas the secondary structure content of the peptide was similar in solution and in the presence of the zwitterionic phospholipid DMPC, it changed significantly in the presence of both DMPG and DMPA, where aggregated structures predominated. Furthermore, CD data reveal that the peptide can adopt a high α-helical content in the presence of lipid mimetic systems. These data suggest that the presence of different phospholipid molecules can modulate the secondary structure of the peptide as has been suggested for other peptides from membrane fusion proteins (*27, 39, 54, 55*). These characteristics would indicate that $SARS_{IFP}$ would interact with the membrane through both electrostatic and hydrophobic effects, as well as it would be adsorbed at the membrane interface changing its conformation depending on the phospholipid headgroups; however, it would be possible that part of the peptide could be inserted deeper than the membrane interface, increasing in this way the membrane permeability. In summary, $SARS_{IFP}$ would interact with negatively charged phospholipids forming β-sheet aggregates accompanied by an increment in phospholipid acyl chain order and headgroup mobility restriction. However, in the absence of negatively charged phospholipids, the peptide would acquire a predominant helical or random conformation and would interact in a more hydrophobic way with the zwitterionic phospholipids, being located in a shallow position with the membrane compromising its integrity. This model should be similar to that suggested in other studies using antimicrobial peptides and amyloid peptides (*56, 57*). Although great progress has been made in the knowledge of the SARS-CoV since its discovery 5 years ago, many aspects of its molecular mechanism are still not totally understood. In this respect, it is outstanding that there is no specific drug or vaccine available to fight against it. This and other segments of the SARS-CoV S2 protein are very attractive candidates for antiviral drug development as well as providing new information for antiviral drug research.

REFERENCES

1. Riley, S., Fraser, C., Donnelly, C. A., Ghani, A. C., Abu-Raddad, L. J., Hedley, A. J., Leung, G. M., Ho, L. M., Lam, T. H., Thach, T. Q., Chau, P., Chan, K. P., Lo, S. V., Leung, P. Y., Tsang, T., Ho, W., Lee, K. H., Lau, E. M., Ferguson, N. M., and Anderson, R. M. (2003) Transmission dynamics of the etiological agent of SARS in Hong Kong: impact of public health interventions. *Science 300*, 1961–1966.
2. Rota, P. A., Oberste, M. S., Monroe, S. S., Nix, W. A., Campagnoli, R., Icenogle, J. P., Penaranda, S., Bankamp, B., Maher, K., Chen, M. H., Tong, S., Tamin, A., Lowe, L., Frace, M., DeRisi, J. L., Chen, Q., Wang, D., Erdman, D. D., Peret, T. C., Burns, C., Ksiazek, T. G., Rollin, P. E., Sanchez, A., Liffick, S., Holloway, B., Limor, J., McCaustland, K., Olsen-Rasmussen, M., Fouchier, R., Gunther, S., Osterhaus, A. D., Drosten, C., Pallansch, M. A., Anderson, L. J., and Bellini, W. J. (2003) Characterization of a novel coronavirus associated with severe acute respiratory syndrome. *Science 300*, 1394–1399.
3. Woo, P. C., Lau, S. K., Chu, C. M., Chan, K. H., Tsoi, H. W., Huang, Y., Wong, B. H., Poon, R. W., Cai, J. J., Luk, W. K., Poon, L. L., Wong, S. S., Guan, Y., Peiris, J. S., and Yuen, K. Y. (2005) Characterization and complete genome sequence of a novel coronavirus, coronavirus HKU1, from patients with pneumonia. *J. Virol. 79*, 884–895.
4. Qinfen, Z., Jinming, C., Xiaojun, H., Huanying, Z., Jicheng, H., Ling, F., Kunpeng, L., and Jingqiang, Z. (2004) The life cycle of SARS coronavirus in Vero E6 cells. *J. Med. Virol. 73*, 332–337.
5. Wang, H., Yang, P., Liu, K., Guo, F., Zhang, Y., Zhang, G., and Jiang, C. (2008) SARS coronavirus entry into host cells through a novel clathrin- and caveolae-independent endocytic pathway. *Cell Res. 18*, 290–301.
6. Li, W., Moore, M. J., Vasilieva, N., Sui, J., Wong, S. K., Berne, M. A., Somasundaran, M., Sullivan, J. L., Luzuriaga, K., Greenough, T. C., Choe, H., and Farzan, M. (2003) Angiotensin-converting enzyme 2 is a functional receptor for the SARS coronavirus. *Nature 426*, 450–454.
7. Wu, X. D., Shang, B., Yang, R. F., Yu, H., Ma, Z. H., Shen, X., Ji, Y. Y., Lin, Y., Wu, Y. D., Lin, G. M., Tian, L., Gan, X. Q., Yang, S., Jiang, W. H., Dai, E. H., Wang, X. Y., Jiang, H. L., Xie, Y. H., Zhu, X. L., Pei, G., Li, L., Wu, J. R., and Sun, B. (2004) The spike protein of severe acute respiratory syndrome (SARS) is cleaved in virus infected Vero-E6 cells. *Cell Res. 14*, 400–406.
8. Follis, K. E., York, J., and Nunberg, J. H. (2006) Furin cleavage of the SARS coronavirus spike glycoprotein enhances cell-cell fusion but does not affect virion entry. *Virology 350*, 358–369.
9. Xiao, X., Chakraborti, S., Dimitrov, A. S., Gramatikoff, K., and Dimitrov, D. S. (2003) The SARS-CoV S glycoprotein: expression and functional characterization. *Biochem. Biophys. Res. Commun. 312*, 1159–1164.
10. Bosch, B. J., van der Zee, R., de Haan, C. A., and Rottier, P. J. (2003) The coronavirus spike protein is a class I virus fusion

protein: structural and functional characterization of the fusion core complex. *J. Virol. 77*, 8801–8811.
11. Xu, Y., Zhu, J., Liu, Y., Lou, Z., Yuan, F., Liu, Y., Cole, D. K., Ni, L., Su, N., Qin, L., Li, X., Bai, Z., Bell, J. I., Pang, H., Tien, P., Gao, G. F., and Rao, Z. (2004) Characterization of the heptad repeat regions, HR1 and HR2, and design of a fusion core structure model of the spike protein from severe acute respiratory syndrome (SARS) coronavirus. *Biochemistry 43*, 14064–14071.
12. Tripet, B., Howard, M. W., Jobling, M., Holmes, R. K., Holmes, K. V., and Hodges, R. S. (2004) Structural characterization of the SARS-coronavirus spike S fusion protein core. *J. Biol. Chem. 279*, 20836–20849.
13. Deng, Y., Liu, J., Zheng, Q., Yong, W., and Lu, M. (2006) Structures and polymorphic interactions of two heptad-repeat regions of the SARS virus S2 protein. *Structure 14*, 889–899.
14. Horvath, C. M., and Lamb, R. A. (1992) Studies on the fusion peptide of a paramyxovirus fusion glycoprotein: roles of conserved residues in cell fusion. *J. Virol. 66*, 2443–2455.
15. Pecheur, E. I., Lavillette, D., Alcaras, F., Molle, J., Boriskin, Y. S., Roberts, M., Cosset, F. L., and Polyak, S. J. (2007) Biochemical mechanism of hepatitis C virus inhibition by the broad-spectrum antiviral Arbidol. *Biochemistry 46*, 6050–6059.
16. Colotto, A., and Epand, R. M. (1997) Structural study of the relationship between the rate of membrane fusion and the ability of the fusion peptide of influenza virus to perturb bilayers. *Biochemistry 36*, 7644–7651.
17. Siegel, D. P., and Epand, R. M. (1997) The mechanism of lamellar-to-inverted hexagonal phase transitions in phosphatidylethanolamine: implications for membrane fusion mechanisms. *Biophys. J. 73*, 3089–3111.
18. Moreno, M. R., Guillen, J., Perez-Berna, A. J., Amoros, D., Gomez, A. I., Bernabeu, A., and Villalain, J. (2007) Characterization of the interaction of two peptides from the N terminus of the NHR domain of HIV-1 gp41 with phospholipid membranes. *Biochemistry 46*, 10572–10584.
19. Moreno, M. R., Giudici, M., and Villalain, J. (2006) The membranotropic regions of the endo and ecto domains of HIV gp41 envelope glycoprotein. *Biochim. Biophys. Acta 1758*, 111–123.
20. Moreno, M. R., Pascual, R., and Villalain, J. (2004) Identification of membrane-active regions of the HIV-1 envelope glycoprotein gp41 using a 15-mer gp41-peptide scan. *Biochim. Biophys. Acta 1661*, 97–105.
21. Ghosh, J. K., Peisajovich, S. G., Ovadia, M., and Shai, Y. (1998) Structure-function study of a heptad repeat positioned near the transmembrane domain of Sendai virus fusion protein which blocks virus-cell fusion. *J. Biol. Chem. 273*, 27182–27190.
22. Samuel, O., and Shai, Y. (2001) Participation of two fusion peptides in measles virus-induced membrane fusion: emerging similarity with other paramyxoviruses. *Biochemistry 40*, 1340–1349.
23. Bosch, B. J., Martina, B. E., Van Der Zee, R., Lepault, J., Haijema, B. J., Versluis, C., Heck, A. J., De Groot, R., Osterhaus, A. D., and Rottier, P. J. (2004) Severe acute respiratory syndrome coronavirus (SARS-CoV) infection inhibition using spike protein heptad repeat-derived peptides. *Proc. Natl. Acad. Sci. U.S.A. 101*, 8455–8460.
24. Guillen, J., Perez-Berna, A. J., Moreno, M. R., and Villalain, J. (2005) Identification of the membrane-active regions of the severe acute respiratory syndrome coronavirus spike membrane glycoprotein using a 16/18-mer peptide scan: implications for the viral fusion mechanism. *J. Virol. 79*, 1743–1752.
25. Sainz, B., Jr., Rausch, J. M., Gallaher, W. R., Garry, R. F., and Wimley, W. C. (2005) Identification and characterization of the putative fusion peptide of the severe acute respiratory syndrome-associated coronavirus spike protein. *J. Virol. 79*, 7195–7206.
26. Petit, C. M., Melancon, J. M., Chouljenko, V. N., Colgrove, R., Farzan, M., Knipe, D. M., and Kousoulas, K. G. (2005) Genetic analysis of the SARS-coronavirus spike glycoprotein functional domains involved in cell-surface expression and cell-to-cell fusion. *Virology 341*, 215–230.
27. Contreras, L. M., Aranda, F. J., Gavilanes, F., Gonzalez-Ros, J. M., and Villalain, J. (2001) Structure and interaction with membrane model systems of a peptide derived from the major epitope region of HIV protein gp41: implications on viral fusion mechanism. *Biochemistry 40*, 3196–3207.
28. Mayer, L. D., Hope, M. J., and Cullis, P. R. (1986) Vesicles of variable sizes produced by a rapid extrusion procedure. *Biochim. Biophys. Acta 858*, 161–168.
29. Böttcher, C. S. F., Van Gent, C. M., and Fries, C. (1961) A rapid and sensitive sub-micro phosphorus determination. *Anal. Chim. Acta 1061*, 203–204.
30. Edelhoch, H. (1967) Spectroscopic determination of tryptophan and tyrosine in proteins. *Biochemistry 6*, 1948–1954.
31. Bernabeu, A., Guillen, J., Perez-Berna, A. J., Moreno, M. R., and Villalain, J. (2007) Structure of the C-terminal domain of the pro-apoptotic protein Hrk and its interaction with model membranes. *Biochim. Biophys. Acta 1768*, 1659–1670.
32. Guillén, J., de Almeida, R. F., Prieto, M., and Villalaín, J. (2008) Structural and dynamic characterization of the interaction of the putative fusion peptide of the S2 SARS-CoV virus protein with lipid membranes, J. Phys. Chem. B 112, 6997–7007.
33. Eftink, M. R., and Ghiron, C. A. (1977) Exposure of tryptophanyl residues and protein dynamics. *Biochemistry 16*, 5546–5551.
34. Sreerama, N., and Woody, R. W. (2000) Estimation of protein secondary structure from circular dichroism spectra: comparison of CONTIN, SELCON, and CDSSTR methods with an expanded reference set. *Anal. Biochem. 287*, 252–260.
35. Sreerama, N., and Woody, R. W. (2004) On the analysis of membrane protein circular dichroism spectra. *Protein Sci. 13*, 100–112.
36. Sreerama, N., and Woody, R. W. (2004) Computation and analysis of protein circular dichroism spectra. *Methods Enzymol. 383*, 318–351.
37. Yeung, K. S., Yamanaka, G. A., and Meanwell, N. A. (2006) Severe acute respiratory syndrome coronavirus entry into host cells: Opportunities for therapeutic intervention. *Med. Res. Rev. 26*, 414–433.
38. Poveda, J. A., Prieto, M., Encinar, J. A., Gonzalez-Ros, J. M., and Mateo, C. R. (2003) Intrinsic tyrosine fluorescence as a tool to study the interaction of the shaker B "ball" peptide with anionic membranes. *Biochemistry 42*, 7124–7132.
39. Pascual, R., Contreras, M., Fedorov, A., Prieto, M., and Villalain, J. (2005) Interaction of a peptide derived from the N-heptad repeat region of gp41 Env ectodomain with model membranes. Modulation of phospholipid phase behavior. *Biochemistry 44*, 14275–14288.
40. Lakowicz, J. (1999) *Principles of Fluorescence Spectroscopy*, Kluwer-Plenum Press, New York.
41. Perez-Berna, A. J., Guillen, J., Moreno, M. R., Bernabeu, A., Pabst, G., Laggner, P., and Villalain, J. (2008) Identification of the membrane-active regions of HCV p7 protein. Biophysical characterization of the loop region, J. Biol. Chem.
42. Lentz, B. R. (1993) Use of fluorescent probes to monitor molecular order and motions within liposome bilayers. *Chem. Phys. Lipids 64*, 99–116.
43. Mantsch, H. H., and McElhaney, R. N. (1991) Phospholipid phase transitions in model and biological membranes as studied by infrared spectroscopy. *Chem. Phys. Lipids 57*, 213–226.
44. Colotto, A., Martin, I., Ruysschaert, J. M., Sen, A., Hui, S. W., and Epand, R. M. (1996) Structural study of the interaction between the SIV fusion peptide and model membranes. *Biochemistry 35*, 980–989.
45. Darkes, M. J., Davies, S. M., and Bradshaw, J. P. (1999) X-ray diffraction study of feline leukemia virus fusion peptide and lipid polymorphism. *FEBS Lett. 461*, 178–182.
46. Aranda, F. J., Teruel, J. A., and Ortiz, A. (2003) Interaction of a synthetic peptide corresponding to the N-terminus of canine distemper virus fusion protein with phospholipid vesicles: a biophysical study. *Biochim. Biophys. Acta 1618*, 51–58.
47. Holland, G. P., McIntyre, S. K., and Alam, T. M. (2006) Distinguishing individual lipid headgroup mobility and phase transitions in raft-forming lipid mixtures with ^{31}P MAS NMR. *Biophys. J. 90*, 4248–4260.
48. Arrondo, J. L., and Goni, F. M. (1999) Structure and dynamics of membrane proteins as studied by infrared spectroscopy. *Prog. Biophys. Mol. Biol. 72*, 367–405.
49. Kielian, M., and Rey, F. A. (2006) Virus membrane-fusion proteins: more than one way to make a hairpin. *Nat. Rev. Microbiol. 4*, 67–76.
50. Schibli, D. J., and Weissenhorn, W. (2004) Class I and class II viral fusion protein structures reveal similar principles in membrane fusion. *Mol. Membr. Biol. 21*, 361–371.
51. Liu, S., Xiao, G., Chen, Y., He, Y., Niu, J., Escalante, C. R., Xiong, H., Farmar, J., Debnath, A. K., Tien, P., and Jiang, S. (2004) Interaction between heptad repeat 1 and 2 regions in spike protein

of SARS-associated coronavirus: implications for virus fusogenic mechanism and identification of fusion inhibitors. *Lancet 363*, 938–947.

52. Ingallinella, P., Bianchi, E., Finotto, M., Cantoni, G., Eckert, D. M., Supekar, V. M., Bruckmann, C., Carfi, A., and Pessi, A. (2004) Structural characterization of the fusion-active complex of severe acute respiratory syndrome (SARS) coronavirus. *Proc. Natl. Acad. Sci. U.S.A. 101*, 8709–8714.
53. Peisajovich, S. G., and Shai, Y. (2003) Viral fusion proteins: multiple regions contribute to membrane fusion. *Biochim. Biophys. Acta 1614*, 122–129.
54. Pascual, R., Moreno, M. R., and Villalain, J. (2005) A peptide pertaining to the loop segment of human immunodeficiency virus gp41 binds and interacts with model biomembranes: implications for the fusion mechanism. *J. Virol. 79*, 5142–5152.
55. Korazim, O., Sackett, K., and Shai, Y. (2006) Functional and structural characterization of HIV-1 gp41 ectodomain regions in phospholipid membranes suggests that the fusion-active conformation is extended. *J. Mol. Biol. 364*, 1103–1117.
56. Bokvist, M., Lindstrom, F., Watts, A., and Grobner, G. (2004) Two types of Alzheimer's beta-amyloid (1−40) peptide membrane interactions: aggregation preventing transmembrane anchoring versus accelerated surface fibril formation. *J. Mol. Biol. 335*, 1039–1049.
57. Zhao, H., Rinaldi, A. C., Di Giulio, A., Simmaco, M., and Kinnunen, P. K. (2002) Interactions of the antimicrobial peptides temporins with model biomembranes. Comparison of temporins B and L. *Biochemistry 41*, 4425–4436.

BI800814Q